ACS Catalysis

pubs.acs.org/acscatalysis Research Article

Electrostatically Regulated Active Site Assembly Governs Reactivity in Nonheme Iron Halogenases

Elizabeth R. Smithwick, R. Hunter Wilson, Sourav Chatterjee, Yu Pu, Joseph J. Dalluge, Anoop Rama Damodaran,* and Ambika Bhagi-Damodaran*

Cite This: ACS Catal. 2023, 13, 13743−13755 Read Online

ACCESS | Metrics & More | Article Recommendations | Supporting Information

ABSTRACT: Non-heme iron halogenases (NHFe-Hals) catalyze the direct insertion of a chloride ion at an unactivated carbon position using a high-valent haloferryl intermediate. Despite more than a decade of structural and mechanistic characterization, a rigorous understanding of the entire catalytic cycle of NHFe-Hals and how they facilitate binding, activation, and reactivity with specific substrates and functionalizing anions remains unclear. Here, we focus on understanding binding and active site assembly in freestanding halogenases, BesD and HalB, which directly catalyze the chlorination of lysine without the need for a partner protein. While the lysine and chloride binding affinities to BesD's active sites are extremely weak (K_d values of ∼50 and 560 mM, respectively), we demonstrate strong positive heterotropic cooperativity (cooperativity constant, $\alpha \sim 15{,}500$) between the lysine and chloride binding events such that they bind efficiently when simultaneously present at physiologically relevant concentrations. Using a combination of computational and rational protein design studies, we identify a negatively charged residue, E119, in BesD that locks the active site assembly unless both the chloride anion and the positively charged lysine substrate are simultaneously present. Removing this electrostatic lock by mutating E119 to polar/neutral glutamine and alanine residues results in a 6.7- and 14-fold increase in affinity for the chloride anion, respectively. A concomitant order of magnitude decrease in chlorination yields is observed as lysine binding is impaired in these mutants, yet the chemoselectivity profile remains rather similar. Beyond such implications for the overall catalytic performance, we show that the electrostatically regulated active site assembly stage of BesD's catalytic cycle can also determine its promiscuity for C−H functionalization with other anions such as bromide, azide, and nitrite. Overall, our studies highlight complex electrostatic effects at play during the active site assembly stage of charged substrates like lysine along with their implications for C−H functionalization performance in BesD-like halogenases.

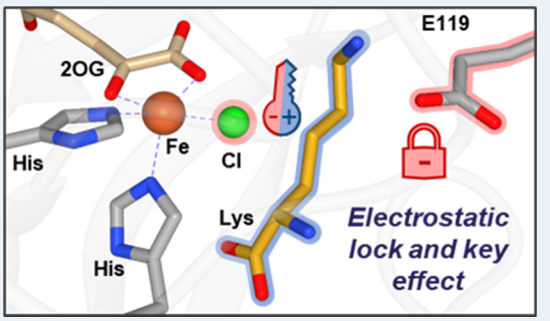

KEYWORDS: *C−H functionalization, iron enzymes, halogenation, cooperative binding, electrostatics*

INTRODUCTION

The use of enzymes as industrial catalysts has gained increasing attention in recent years for their ability to achieve complex chemical transformations with a high degree of regio- and stereoselectivity under environment-friendly conditions.[1−6] Non-heme iron halogenases (NHFe-Hals), in particular, hold great value as biocatalytic platforms as they are able to install a chloride moiety at an unactivated sp^3-hybridized carbon in a selective manner (Figure 1A).[7−12] Conforming to the literature on non-heme iron enzymes, we use the term "substrate" in this work to strictly refer to the molecule that is the subject of C−H functionalization.[10,13−15] NHFe-Hals enable regio- and stereoselective chlorination of their native substrates using chloride, 2-oxoglutarate (2OG), and oxygen as cosubstrates with desired product ratios as high as 95%.[16] NHFe-Hals have also been shown to enable C−H functionalization with non-native anions including bromide, azide, and nitrite, albeit with significantly reduced yields.[9,10,12] A major challenge with NHFe-Hals, however, is that their substrate scope is rather limited as most known NHFe-Hals require their substrates to be attached to a partner protein.[13,17−23] Only a handful of identified NHFe-Hals are able to act on freestanding substrates, limiting their substrate scope currently to some amino acids,[7] alkaloids,[11,24] and nucleotides[25] (Figure 1A). A frequently used strategy to counteract the limited substrate scope of NHFe-Hals has been to engineer a related class of better-characterized enzymes called non-heme iron hydroxylases (NHFe-Hyds) which offer a broader range of substrates.[26−28] NHFe-Hals and NHFe-Hyds differ in their primary coordination sphere (PCS) seemingly by a single amino acid substitution, with NHFe-Hyds featuring a canon-

Received: June 3, 2023
Revised: September 25, 2023
Published: October 11, 2023

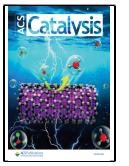

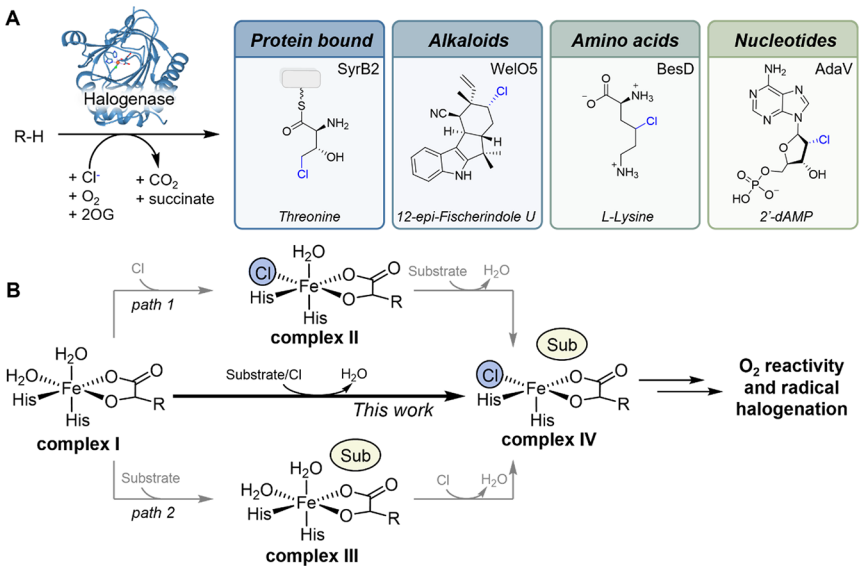

Figure 1. (A) Simplified halogenation reaction and current substrate scope of NHFe-Hals with specific examples of each substrate category. (B) Schematic showing complexes formed to significant levels in NHFe-Hals at physiological concentrations of chloride and substrate.

ical 2-His-1-carboxylate facial triad that coordinates to the iron center.[29] In NHFe-Hals, however, the carboxylate of the facial triad is substituted for a glycine or alanine, allowing an open coordination position for chloride to bind.[30] Initial attempts to reprogram NHFe-Hyds into halogenases by this single amino acid substitution of Glu/Asp to Ala/Gly were unsuccessful in achieving the desired chemoselectivity, indicating a more complex molecular mechanism at play.[31−33] This motivated several experimental and computational studies to explore the factors determining the chemoselectivity of NHFe-Hals and engineered NHFe-Hyds. These factors include the configuration of the haloferryl isomer[34−37] and the oxo-Fe−H angle that it forms with the target C−H group,[38] the optimal positioning of the substrate radical in relation to the chloride ligand of the Cl−Fe^{III}−OH intermediate,[16,39,40] as well as protein pocket electrostatics that can facilitate chloride transfer.[41,42] While most of these studies have focused on the oxygen activation, C−H abstraction, and chloride transfer stages of the catalytic cycle (Figure S1), how catalytic pocket electrostatics can control the active site assembly when working with charged and untethered substrates like free lysine and functionalizing anions like chloride, along with their implications for the overall catalytic performance and product yields, remains unexplored. Thus, a more rigorous understanding of the entire catalytic cycle and how NHFe-Hals facilitate binding, activation, and reactivity with specific substrates and functionalizing anions is needed.

The current understanding of binding events in halogenases has been built off of comparisons to NHFe-Hyds as well as studies on HctB, SyrB2, and CytC3 halogenases that catalyze halogenation on protein-tethered molecules.[14,43−48] In the absence of substrate and chloride, the iron center in NHFe-Hals is six-coordinate (6*c*) with two histidines, two aqua ligands, and 2OG comprising the PCS (complex **I** in Figure 1B). This unreactive complex **I** converts to the catalytically primed complex **IV** in a random sequential order of chloride- and substrate-binding events (path 1 or 2, Figure 1B). Once formed, the substrate- and chloride-bound complex **IV** will react rapidly with O_2 to form a high-valent haloferryl intermediate that abstracts a hydrogen atom from the substrate.[49] The newly formed substrate radical can then rebind with iron-coordinated chloride to form the chlorinated product.[16,40] In this work, we focus on understanding the active site assembly and the impacts that it has on the catalysis of freestanding halogenases, BesD and HalB, which directly catalyze the chlorination of free lysine. Our studies reveal a strong positive heterotropic cooperativity (cooperativity constant, $\alpha \sim 15{,}500$) in the binding of positively charged lysine and the chloride anion during the active site assembly stage. Through detailed computationally guided rational protein design studies, we highlight the role of a negatively charged E119 residue in BesD's secondary coordination sphere (SCS) that electrostatically locks the active site assembly unless both the chloride anion and the positively charged lysine substrate are simultaneously present. We show that changes to active site electrostatics by mutating E119 to polar/neutral Gln/Ala residues result in order-of-magnitude changes to the chloride- and lysine-binding affinities, along with a significant dip in chlorination yields, yet with rather similar chemoselectivity profiles. Such complex electrostatic effects at play during the active site assembly of BesD also determine its promiscuity to bind and react with other functionalizing anions such as bromide, azide, and nitrite. Overall, our studies reveal the crucial role of pocket electrostatics in the active site assembly and catalytic performance of BesD-like enzymes that act upon untethered charged substrates such as free lysine and utilize anions such as chloride for C−H functionalization reactions.

MATERIALS AND METHODS

Protein Expression and Purification. The plasmid for His10-tagged *Streptomyces lavenduligriseus* BesD and *Streptomyces wuyuanensis* HalB contained in a pET16b vector was received as a gift from Chang lab (UC Berkeley) and sequenced to confirm gene integrity. The plasmids were transformed to Rosetta 2 (DE3) cells for protein overexpression. Colonies from an overnight LB-agar plate containing carbenicillin (50 μg/mL) and chloramphenicol (37 μg/mL) were inoculated into 250 mL flasks containing TB media (50 mL) with the same concentrations of antibiotics and

https://doi.org/10.1021/acscatal.3c02531
ACS Catal. 2023, 13, 13743−13755

incubated at 37 °C overnight at 200 rpm. Culture flasks with TB (1.5 L) and appropriate antibiotics were inoculated with overnight cultures and grown at 37 °C at 200 rpm until cells reached an OD_{600} of 0.9−1.1. Upon reaching appropriate optical densities, the cultures were cooled on ice for 15 min before the addition of IPTG (0.25 mM) and then incubated at 16 °C for 24 and 18 h for BesD and HalB, respectively. After overexpression, cells were collected by centrifugation at 8000 rpm at 4 °C, flash-frozen, and stored at −20 °C for further use.

The frozen cells were resuspended in lysis buffers (50 mM HEPES, 300 mM NaCl, 10 mM imidazole, 1 mM $CaCl_2$, 25 mM $MgCl_2$, 0.1 mg/mL RNase, and 0.1 mg/mL DNase, pH = 7.5) and then lysed by sonication. The lysed cell solution was centrifuged to separate out insoluble cell debris, and then the supernatant was collected and filtered through 0.45 μm filters. The filtered supernatant was applied to a 5 mL HisTrapFF column using an AKTA Start protein purification system. After sample application, the column was washed with 15 column volumes (CVs) of wash buffer (50 mM HEPES, 300 mM NaCl, 10 mM imidazole, and 20 mM 2-mercaptoethanol, pH = 7.5), and then the His-tagged protein was eluted using a two-step gradient method first with 45% elution buffer (50 mM HEPES, 300 mM NaCl, 300 mM imidazole, and 20 mM 2-mercaptoethanol, pH = 7.5) for eight CVs to remove nonspecific interacting proteins, which was then increased to 100% elution buffer to elute high-purity protein for eight CVs. Fractions from the last elution step were collected and dialyzed in 50 mM HEPES, 100 mM NaCl, 1 mM DTT, and 1 mM EDTA (pH = 7.5) for 2 h and then transferred to a dialysis buffer of 50 mM HEPES, 1 mM DTT, and 100 mM NaCl (pH = 7.5) for 2 h. After this second round of dialysis, the protein solution was diluted to a concentration of 0.02−0.05 mM and then incubated with HRV-3C protease (1 mg protease to 100 mg protein), dialyzing against 50 mM HEPES, 1 mM DTT, and 100 mM NaCl (pH = 7.5) overnight. The protein was then concentrated to approximately 10 mL using an Amicon Ultra-15 centrifugal filter (10 kDa MWCO), and then imidazole was added to the protein solution to a final concentration of 10 mM. The protein solution was applied to a 5 mL HisTrapFF column using an AKTA Start protein purification system. His-tagged cleaved BesD was recovered during sample application and subsequent four CV wash with the wash buffer. Protease and residual His-tagged protein were eluted with elution buffer. The collected fractions were concentrated, and then the protein was applied to a PD-10 desalting column equilibrated with 50 mM HEPES (pH = 7.5). Fractions were collected based on absorbance at 280 nm. The collected fractions were further concentrated, and glycerol (15%) was added to the protein solution for storage. The BesD and HalB purity and His-tag cleavage were confirmed via gel electrophoresis and mass spectrometry. The protein solution was aliquoted, flash-frozen, and stored at −80 °C for further use.

Site-Directed Mutagenesis. Site-directed mutagenesis was performed on pET16b BesD plasmid to create E119A and E119Q mutations using the Phusion site-directed mutagenesis kit from Thermo Scientific. The forward and reverse primers (5′ to 3′) for the E119A mutant were CAAGGCCGACGCGGAATTCCTC and GGGCAGGGGTGCAGTTTCTCG, respectively, and the forward and reverse primers (5′ to 3′) for the E119Q mutant were CAAGGCCGACCAGGAATTCCTCATC and GGGCAGGGGTGCAGTTTCTCG, respectively. A two-step protocol of denaturation, followed by combined annealing−extension was performed for both mutants in an Axygen MaxyGene II instrument with an annealing temperature of 72.0 °C. PCR products were transformed into DH5α cells for plasmid expression. Single mutant DNA sequences were confirmed using Sanger sequencing by ACGT DNA sequencing services.

Anaerobic Equilibrium UV−Vis Studies. All UV−Vis studies were performed anaerobically on a Cary60 UV−Vis spectrophotometer at 11 °C. Anaerobic solutions of 100 mM HEPES (pH = 7.5) and 100 mM 2OG in 100 mM HEPES (pH = 7.5) were prepared through alternating cycles of vacuum degassing, followed by argon flushes. Dry solids for all other compounds were brought into the anaerobic glovebag environment, and solutions were prepared with the O_2-free solution stocks. Before each UV−Vis experiment, BesD or HalB was buffer-exchanged three times into O_2-free 100 mM HEPES (pH = 7.5) in 0.5 mL Amicon Ultra 10 kDa MWCO centrifugal filter units by centrifugation at 13,500 rpm for 20 min at 4 °C. A solution of BesD or HalB was prepared in a cuvette to a final concentration of 0.13 mM ± 0.02. Aliquots of $(NH_4)_2Fe(SO_4)_2$ in water, 2OG in 100 mM HEPES, NaX (X = Cl, Br, N_3, or NO_2) in 100 mM HEPES, and L-lysine in 100 mM HEPES were added sequentially to the protein solution to the final concentrations of 97.5 μM $(NH_4)_2Fe(SO_4)_2$, 630 μM 2OG, 5 mM NaX (X = Cl, Br, N_3, NO_2), and 5 mM L-lysine. Stock solutions of each compound were prepared so that small aliquots could be added to the cuvette to keep the volume change below 10%. Multiple spectra were acquired 10 min after each component addition to ensure stable analyte signals. All spectra shown are background-corrected by the average signal of 775−800 nm and dilution-corrected unless otherwise stated. Titrations were performed analogous to UV−Vis addition experiments. For lysine concentrations of 150 μM and above, the final concentrations in the cuvette before the addition of chloride titrant solutions were 330 ± 20 μM BesD, 600 μM $(NH_4)_2Fe(SO_4)_2$, and 800 μM 2OG in 100 mM HEPES (pH = 7.5) at the lysine concentrations indicated in figures. For titrations in the absence of lysine, final concentrations in the cuvette before the addition of chloride titrant solutions were 350 ± 10 μM BesD, 1 mM $(NH_4)_2Fe(SO_4)_2$, and 1.5 mM 2OG in 100 mM HEPES (pH = 7.5), and the volume was significantly altered during the course of the titration but accounted for in dilution corrections. Increases in absorbance at 518 nm were converted into fractions of chloro-bound protein by dividing the titrant absorbance value by the theoretical max, and the resulting scaled data were fit using the quadratic binding equation for titrations with lysine of 150 μM and above and the hyperbolic binding equation for lysine-absent chloride titrations.

Equilibrium Dialysis Studies. All equilibrium dialysis experiments were conducted anaerobically. To prepare the protein, BesD was brought into a glovebag and buffer-exchanged three times into an O_2-free 50 mM HEPES (pH = 7.5) as described previously. Stock solutions of compounds were prepared as described in the previous section. Protein solutions of 400−450 μM BesD, 4 mM 2OG, 1 mM $(NH_4)_2Fe(SO_4)_2$, 0 or 5 or 30 mM NaCl, and 45 or 42.5 or 35 mM Na_2SO_4 in 50 mM HEPES (pH = 7.5) were dialyzed against an equal volume of lysine-containing solution (125−1000 μM) in 4 mM 2OG, 1 mM $(NH_4)_2Fe(SO_4)_2$, 0 or 5 or 30 mM NaCl, 45 or 42.5 or 35 mM Na_2SO_4, and 50 mM HEPES (pH = 7.5) for 20 h. The concentrations of NaCl and

https://doi.org/10.1021/acscatal.3c02531
ACS Catal. 2023, 13, 13743−13755

Na_2SO_4 depended on the identified experiment, as detailed in Figure S4. After 20 h, 50 μL of samples from the nonprotein chamber was combined with 40 μL of 30 mM borate buffer (pH = 10.5), and then amino acids were derivatized with 10 μL of ca. 10 mM 6-aminoquinolyl-*N*-hydroxysuccinimidylcarbamate (AQC) in acetonitrile. Immediately after the derivatizing agent was added, the samples were vortexed for 10 s. Samples with initial lysine concentrations of 800−1000 μM were diluted twofold, and 50 μL from the diluted sample was derivatized and analyzed. The dialysis samples for mutants were run analogous to WT BesD but for only one concentration of starting lysine (1 mM in a protein-free chamber before equilibration), with the background buffer containing 4 mM 2OG, 1 mM $(NH_4)_2Fe(SO_4)_2$, 30 mM NaCl, and 35 mM Na_2SO_4 in 50 mM HEPES (pH = 7.5).

Derivatized amino acid samples were then run on a Shimadzu Prominence-i LC-2030C 3D Plus system equipped with a Regis Technologies REXCHROM C18 column (4.60 mm × 250 mm × 5 μm) and a PDA detector. Separations occurred with a gradient separation at a temperature of 35 °C, an injection volume of 25 or 50 μL (specific injection volumes are indicated in relevant figure captions), and a flow rate of 0.5 mL/min. The separation method is as follows: 0% B to 70% B, 0.0 to 40.0 min; 70% B to 100% B, 40.0 to 42.0 min; 100% B, 42.0 to 50.0 min; 100% B to 0% B, 50.0 to 52.0 min; 0% B, 52.0 to 60.0 min, where solution A is 5 mM ammonium acetate (pH = 5.0) and solution B is 60% acetonitrile in water. All HPLC traces were constructed from the absorbance at 254 nm. Peak areas were converted to concentrations through a standard curve (Figure S3) to determine the free lysine concentration in each equilibrium dialysis sample, allowing the data to be fit by the hyperbolic binding equation.

Stopped-Flow UV−Vis Spectroscopy. Protein solutions for stopped-flow studies were prepared similar to equilibrium studies. Before stopped-flow mixing, the final solutions of anaerobic protein solutions were 225 μM BesD, 2.25 mM lysine, 10 mM NaCl, 170 μM $(NH_4)_2Fe(SO_4)_2$, and 2.25 mM 2OG in 100 mM HEPES (pH = 7.5) unless the experiment indicates a component was absent during the measurement. Room-temperature O_2-saturated solutions of 100 mM HEPES (~1 mM O_2) were prepared by bubbling O_2 gas through the solution for several hours. Stopped-flow was run on an Applied Photophysics SX-20 system paired with an Ocean Optics detector triggered through a Siglent waveform generator. Equal volumes of the prepared anaerobic protein solution and O_2-saturated buffer were combined at 11 °C in an anaerobic glovebag.

Molecular Dynamics. The homology model for BesD from *Streptomyces lavenduligriseus* was created using the SWISS-MODEL tool[50] with default parameters from the crystal structure of BesD from *Streptomyces cattleya* which shares 75% identity with the target protein.[50−55] Hydrogen atoms were added to the homology model at a pH of 7.5 with the H++ Web server.[56−58] Using the tleap module in AMBER 20, BesD was parametrized with the ff19SB force field, 2OG was parametrized using GAFF (charges were assigned with the antechamber module), and iron was described as a ferrous species.[59−63] The protein was solvated in a 10.0 Å OPC water box, and Na^+ and Cl^- ions were added to neutralize the system.[64] The substrate lysine was treated as a zwitterionic species with a charged epsilon amine.[65] All varying coordination systems were created manually by editing input pdb files prior to the creation of AMBER input files with the tleap module. The systems representing the varied coordination states were minimized (first solvent and then protein) and gently heated to 300 K, and the density was equilibrated for 2 ns. For each coordination system, three independent 250 ns production runs were performed. To maintain the primary coordination sphere of iron in the six-coordinate systems, all ligand distances were restrained to within 0.1 Å of their crystallographic distances using a force constant of 100.0 kcal mol^{-1} $Å^{-1}$. For MD simulations involving the five-coordinate (5*c*) species, the iron−ligand bonds and angles were treated explicitly using parameters developed from the MCPB Python package in AmberTools21.[66,67] For all MCPB calculations, the B3LYP/6-31G(d) level of theory was employed.[68−70] During geometry optimizations, the α-carbons of all amino acids and C5 of the 2OG ligand were held fixed to mimic their positions within the protein structure. Trajectory analyses were performed with CPPTRAJ; H-bond donor−acceptor cutoff distances were set to 3.2 Å.[71] Error bars in the analysis were calculated using the standard error over the independent simulations (standard deviation divided by $\sqrt{n}$).[72]

DFT Calculations. All electronic structure calculations were performed with the ORCA software package (version 5.0.3).[73,74] All geometry optimizations were conducted at the B3LYP-D3BJ/def2-SVP level of theory; iron and all coordinating atoms in the primary coordination sphere were treated with the def2-TZVP basis set.[68,69,75−78] Revised BJ damping parameters were employed to prevent overcorrection of the treatment of dispersion interactions.[79] The resolution of identity approximation for Coulomb and numerical chain-of-sphere integration for exchange integrals (keyword: RIJCOSX) was used to accelerate all geometry optimizations. The auxiliary basis def2/J was called for all geometry optimizations.[80] The keyword "defgrid2" was used to build all integration grids, and the keywords "SOSCF" and "SlowConv" were used to aid the SCF convergence.

Representative snapshots from each MD trajectory, where E119 was a median distance away from the iron center, were taken as the input to build DFT models for different active site configurations. The model systems include iron, all ligands coordinated to it, substrate lysine, and protein residues N218 and E119. All protein residues were truncated and capped at the α-carbon. 2OG was truncated to pyruvate to prevent unphysical interactions during geometry optimizations. The α-carbons of all amino acid residues and the methyl carbon of pyruvate were held fixed during the geometry optimization. The protein environment was simulated by using a dielectric constant of ε = 4 using the CPCM solvation model. After geometry optimization, the Multiwfn package was used to calculate RESP charges through a two-step procedure and then used to generate electron density and electrostatic potential surfaces.[81−83] The resulting surfaces were visualized in VMD with a surface isovalue of 0.02 and the color scale data range set to 0.20 to −0.20.[84]

Activity Assays. For reactions containing non-native anions, all reactions were prepared anaerobically. BesD was brought into a glovebag after six antechamber cycles and allowed to equilibrate in an anaerobic environment for 1 h. For non-native anion reactions, BesD (final concentration: 50 μM) was combined with 10 mM anion salt (NaBr, NaN_3, or $NaNO_2$), 5 mM 2OG, 1 mM sodium ascorbate, 100 μM $(NH_4)_2Fe(SO_4)_2$, and 200 μM lysine. All samples were brought out of the glovebox and exposed to oxygen to initiate reactions. Reactions containing azide and nitrite were

https://doi.org/10.1021/acscatal.3c02531
ACS Catal. 2023, 13, 13743−13755

incubated in an Eppendorf Thermomixer at 23 °C, mixing overnight (350 rpm). Due to the observed instability of the brominated species, reactions containing bromide were incubated in an Eppendorf Thermomixer at 4 °C, mixing for 1 h (350 rpm). For mutant BesD reactions, all reactions were performed aerobically. The reaction samples contained either WT BesD, E119A, or E119Q at a final concentration of 10 μM BesD in 5 mM NaCl, 5 mM 2OG, 1 mM sodium ascorbate, 100 μM $(NH_4)_2Fe(SO_4)_2$, and 200 μM lysine. Reactions were incubated in an Eppendorf Thermomixer at 23 °C, mixing for 4 h (350 rpm).

After incubations, all reactions were filtered through 0.5 mL Amicon Ultra 10 kDa MWCO centrifugal filter units at 13,500 rpm for 20 min at 4 °C. Reaction flowthrough (135 μL) was collected for further processing from each reaction. The collected reaction flowthrough samples (135 μL) were combined with 20 μL of 100 mM sodium tetraborate (pH = 8.5), 5 μL of 200 μM of L-lysine (13C6, 99%; 15N2, 99%)·2HCl, 1.5 μL 5 M NaOH, and 18.5 μL of Milli-Q H_2O. AQC in acetonitrile was added to each reaction mixture to a final concentration of ca. 1 mM and a total sample volume of 200 μL. The samples were vortexed immediately after AQC addition. To analyze the reaction product distributions, the reaction samples were run on a Waters Acquity UPLC system coupled to a Waters triple quadrupole mass spectrometer (Acquity TQD). Column choice, gradient method, and instrument parameters were adapted from previous studies.[36] The mass transitions monitored for each reaction are listed in Table S1.

Accurate Mass Determination of BesD Enzymatic Products. A Sciex Exion UHPLC coupled to a Sciex X500R quadrupole time-of-flight (qtof) mass spectrometer was used for the separation and accurate mass measurement of AQC-derivatized BesD enzymatic products. A Waters CORTECS UPLC C18 2.1 mm × 100 mm column (1.6 μm particles) at 55 °C was used during the following 10 min gradient separation, with A: water containing 0.1% formic acid and B: ACN containing 0.1% formic acid, at a flow rate of 0.5 mL/min: 1% B, 0 to 1.0 min; 1% B to 13% B, 1.0 to 2.0 min; 13% B to 15% B, 2.0 to 5.5 min; 15% B to 95% B, 5.5 to 6.5 min; 95% B, 6.5−7.5 min; 95% B to 1% B, 7.5−7.7 min; and 1% B, 7.7 to 10 min. Electrospray ionization mass spectra in positive ionization mode were collected over the range of m/z 50−1200 during the analysis. MS parameters were as follows: ion source gas 1:45 psi; ion source gas 2:45 psi; curtain gas: 30 psi; CAD gas: 7; temp: 500 °C; spray voltage: 550 V; declustering potential: 50 V; DP spread: 0 V; CE: 10 V; CE spread: 0 V.

Bioinformatics. Sequences for BesD-like halogenases and hydroxylases were acquired by using the sequence of *Streptomyces lavenduligriseus* BesD as a query sequence for a BLAST search within the nonredundant protein database with an expectation value cutoff of 1×10^{-5}. This resulted in 698 sequences which were then aligned using the MUSCLE algorithm.[85] After initial alignment, the sequences were sorted into hydroxylases and halogenases based on the HXG/A motif for halogenases and the HXD/E motif for hydroxylases. The sorted sequences were then filtered using the CD-hit algorithm to remove sequences with a 90% similarity cutoff, leading to 119 halogenase sequences and 241 hydroxylase sequences.[86,87] The filtered sequence sets for halogenases and hydroxylases were realigned using the MUSCLE algorithm, and LOGOS plots were created using WebLogo (https://weblogo.berkeley.edu/logo.cgi).[88]

RESULTS AND DISCUSSION

We began our studies to understand how lysine and chloride bind to the active site of BesD by using UV−Vis spectroscopy. NHFe-2OG-dependent enzymes exhibit a broad metal-to-ligand charge-transfer (MLCT) band between the Fe^{II} center and the bidentate-coordinated 2OG ligand centered around 475−550 nm.[89] This spectral feature is sensitive to changes in the PCS of iron and has been used to study substrate binding in NHFe-Hyds and functionalizing anion binding in NHFe-Hals.[10,31,46,89−92] Upon the addition of Fe^{II} and 2OG to BesD, an MLCT band forms, with the peak maximum centered at 480 nm (Figure 2A, dark purple spectrum) that can be assigned to a *6c*-diaqua Fe species (**I**), similar to the complex previously characterized in SyrB2.[10] However, unlike SyrB2 and other non-heme iron enzymes,[10,31] the peak maximum of the MLCT band remains mostly unperturbed upon the addition of chloride to the BesD-Fe-2OG complex even at 4.5 mM excess concentrations (Figure 2A, light purple spectrum). It is not until lysine is added to the chloride-containing mixture that a distinctive shift in peak maximum to 500 nm is observed (Figure 2A, teal spectrum), indicating that a change in the PCS of iron has occurred. After reversing the order of chloride and lysine additions, we now find that the addition of only lysine (4.5 mM excess) induces hardly any spectral shift, in contrast to other characterized NHFe enzymes.[46,47,89] Only after the addition of chloride to the BesD-Fe-2OG-lysine mixture does the peak maximum shift, indicating that both lysine and chloride work in tandem to alter the PCS of Fe^{II} (Figure 2B). To investigate the catalytic relevance of complex **I** and various lysine- and chloride-added forms of BesD, we employed stopped-flow UV−Vis spectroscopy[93−95] to explore their O_2 reactivity profiles by monitoring the formation of the high-valent ferryl intermediate (Fe^{IV}=O) through transient absorbance increases at ∼320 nm, as has been established previously.[10,44,90] Analogous to these studies, we observe a rapid increase in absorbance at 320 nm when the BesD-Fe-2OG-Lys-Cl complex is mixed with O_2-saturated buffer (∼1 mM O_2), indicating an efficient reaction with oxygen (Figure 2C, teal curve). Based on such a reactivity profile, we assign the BesD-Fe-2OG-Lys-Cl complex with MLCT centered at 500 nm (Figure 2A,B, teal spectrum) to be the catalytically primed *5c*-chloro Fe complex **IV**. In contrast, if either chloride and/or lysine are absent, the protein complex exhibits negligible reactivity with O_2 (Figure 2C, gray/purple/green spectrum). The minor initial reactivity observed in the lysine-only condition is likely due to chloride contamination, as seen in previous studies.[10,12] In all, UV−Vis studies combined with stopped-flow kinetic investigations reveal that both lysine and chloride cooperatively bind to convert complex **I** to a catalytically primed complex **IV** in BesD (Figure 2D). We note that the peak shift in the MLCT band, upon simultaneous addition of lysine and chloride, represents such a conversion (Figure 2A,B). Furthermore, we observe similar trends in HalB (Figure S2), suggesting that this effect could be a common mechanism across the lysine-halogenating NHFe-Hals.

Having uncovered the synergistic effects in the binding of lysine and chloride to BesD, we conducted binding affinity studies to further explore the nature of their association with the protein. First, we used an equilibrium dialysis approach in tandem with HPLC-based quantification of free lysine concentrations to acquire apparent lysine-binding affinities ($K_{d,app}^{Lys}$). For these experiments, approximately 0.45 mM BesD

https://doi.org/10.1021/acscatal.3c02531
ACS Catal. 2023, 13, 13743−13755

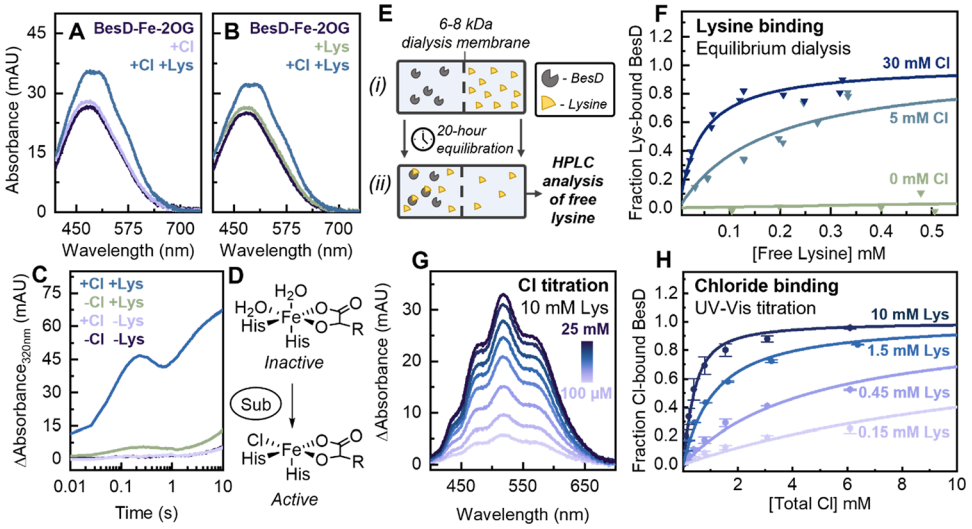

Figure 2. Spectral changes in the MLCT band of the BesD-Fe-2OG complex (130 ± 5 μM BesD, 97.5 μM Fe, and 630 μM 2OG in 100 mM HEPES (pH = 7.5)) upon sequential additions of (A) 5 mM Cl and then 5 mM lysine or (B) 5 mM lysine and then 5 mM Cl. (C) Stopped-flow UV−Vis spectroscopic kinetic studies investigating the change in absorbance at 320 nm over time for various combinations of lysine/chloride. A rapid (<100 ms) absorbance increase at 320 nm in non-heme iron enzymes is the signature of ferryl intermediate formation. (D) Conversion of complex **I** to a catalytically primed complex **IV** in BesD upon cooperative binding of lysine and chloride. (E) Schematic showing the setup of equilibrium dialysis. (i) Initial equilibrium dialysis configuration, where protein is on one side of the dialysis membrane and lysine is added to the other side. (ii) After a 20 h equilibration period, lysine diffused through to both equilibrium dialysis chambers, and the sample is taken from the protein-free side to measure the free lysine concentrations. (F) Equilibrium dialysis-based binding studies of lysine to BesD-Fe-2OG at 30 mM NaCl, 5 mM NaCl, and 0 mM NaCl (n = 2). (G) Difference spectra upon chloride additions (0.1−25 mM) to the BesD-Fe-2OG complex at 10 mM lysine, where the initial 0 mM Cl spectra has been subtracted from subsequent chloride additions. (H) Titration curves for chloride at different total lysine concentrations where the increasing absorbance of 518 nm from the difference spectra has been converted to the fraction of chloride-bound BesD (n = 2).

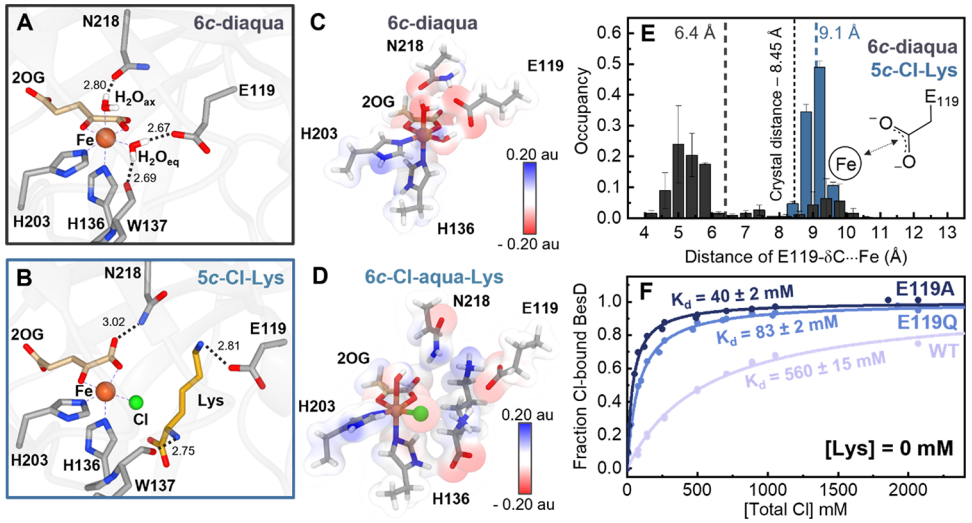

Figure 3. Representative structures of MD-simulated (A) 6*c*-diaqua complex **I** and (B) 5*c*-Cl-Lys complex **IV** in BesD. Electrostatic potential surfaces calculated based on the RESP charges of optimized representative MD snapshots of (C) 6*c*-diaqua complex **I** and (D) 6*c*-Cl-aqua Lys complex in WT BesD. The aqua ligand in (D) was added back before the geometry optimization for more consistent comparisons between surfaces. (E) Histogram of the distance between iron and the δ-carbon of E119 computed during the simulation of the different active site configurations. Dotted lines represent the median distance averaged between triplicate simulations. (F) UV−Vis spectroscopy-based titration curves for chloride for WT, E119Q, and E119A BesD at 0 mM lysine concentrations (n = 2).

was dialyzed against varying concentrations of lysine (0.125−1 mM) at 0, 5, and 30 mM chloride concentrations to obtain a series of apparent lysine-binding affinity curves (Figure 2E,F). In the absence of any chloride, we observed negligible lysine binding to BesD even at free lysine concentrations as high as 0.5 mM (Figures 2F and S4), suggesting a weak binding affinity for lysine (K_d^{Lys}) in the high millimolar range. Upon increasing the total chloride concentrations to 5 and 30 mM, we measure the systematically enhanced apparent binding affinities with $K_{d,app}^{Lys}$ values of 0.17 ± 0.02 and 0.043 ± 0.003 mM, respectively. Such enhanced apparent lysine-binding affinity with increasing chloride concentrations is strong evidence for the positive heterotropic cooperativity between the lysine- and chloride-binding events. Next, as a comple-

https://doi.org/10.1021/acscatal.3c02531
ACS Catal. 2023, 13, 13743−13755

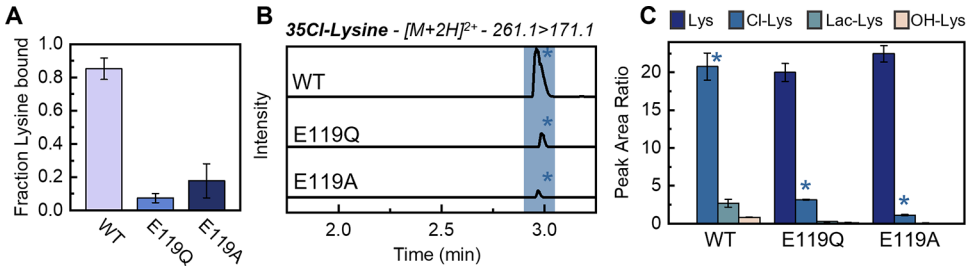

Figure 4. (A) Fraction of lysine-bound species detected for 425 ± 25 μM WT, E119A, or E119Q BesD with 30 mM NaCl when 1 mM lysine was allowed to equilibrate for 20 h between the top and bottom chambers of equilibrium dialysis apparatus. (B) MRM chromatograms corresponding to ^{35}Cl−lysine mass transition for reactions of 10 μM WT, E119Q, or E119A containing 5 mM 2OG, 1 mM sodium ascorbate, 100 μM $(NH_4)_2Fe(SO_4)_2$, 5 mM NaCl, and 200 μM lysine in 100 mM HEPES (pH = 7.5). (C) Peak area ratios (analyte/$^{13}C_6$,$^{15}N_2$-lysine internal standard) observed for unreacted lysine and reaction product distributions of WT, E119Q, and E119A. All detected products were AQC-derivatized analytes.

mentary technique to explore such cooperative binding phenomena, we conducted UV−Vis-based chloride titration assays to acquire apparent chloride-binding affinity values ($K_{d,app}^{Cl}$) at varying lysine concentrations. The absorbance change in the UV−Vis MLCT band upon chloride-binding to iron allows quantitation of the chloride-bound fraction of BesD (Figures 2G and S5). These UV−Vis-based chloride titration experiments reveal systematically enhanced apparent chloride-binding affinities ($K_{d,app}^{Cl}$) of 14.8 ± 1.4, 4.5 ± 0.4, 0.99 ± 0.05, and 0.22 ± 0.02 mM, with increasing total lysine concentrations of 0.15, 0.45, 1.5, and 10 mM, respectively (Figure 2H). Overall, the enhanced apparent chloride-binding affinity with increasing lysine concentrations measured using UV−Vis approaches in tandem with the enhanced apparent lysine-binding affinity with increasing chloride concentrations measured via equilibrium dialysis confirm the positive heterotropic cooperativity in the binding of lysine and chloride to BesD's catalytic core. The $K_{d,app}^{Cl}$ values obtained at various lysine concentrations enable us to perform an exact analysis of heterotropic cooperative binding in BesD to estimate the cooperativity constant ($\alpha \sim 15{,}500$; see calculations and equations used in Figure S6 and further discussion in Supporting Information).[96] Such a high α value is indicative of strong positive heterotropic cooperativity effects at play during the lysine- and chloride-binding events during the active site assembly in BesD. These studies also suggest that lysine and chloride bind BesD effectively only when simultaneously present at physiologically relevant concentrations[97] of 0.3−0.8 and 6−50 mM, respectively.

In order to probe the molecular basis of such a strong cooperativity, we performed MD simulations on different BesD active site configurations. In simulations with the 6*c*-diaqua BesD-Fe complex **I**, we observe a strong hydrogen bonding (H-bonding) network composed of E119 and W137 that stabilizes the equatorial-aqua ligand (Figure 3A). We find that both of these residues are highly conserved in the BesD family of halogenases, with glutamate/aspartate present in >95% sequences at 119 position and W137 present in all of the sequences (Figure S7). Moreover, both residues have been found to play an important role in BesD's halogenation catalytic efficiency. Specifically, the mutation of E119 to an Ala was shown to result in a loss of activity, and W137 was found to impose the proper substrate angle for halogenation reactivity.[7,38] Our simulations show that the H-bond network formed by these residues in 6*c*-diaqua complex **I** undergoes a dramatic reorganization upon binding chloride and lysine to form the 5*c*-Cl-Lys complex **IV** (Figures 3B and S8). Comparing the two configurations, we observe that lysine forms a salt-bridge with the E119 residue which necessitates disruption of the rather strong H-bond (sampled over 73 ± 22% of the simulation) between E119 and iron's equatorial-aqua ligand creating an energy barrier to lysine binding. The presence of chloride at the equatorial site will not only help disrupt these H-bonds but also provide favorable electrostatic interactions for lysine binding. Similarly, the negative charge on E119 near the active site would repel chloride until screened by positively charged lysine. By generating electrostatic potential surfaces based on the optimized geometries of MD simulations, we can see that the presence of E119 creates a negative potential at the equatorial site in the absence of lysine, as indicated by the red color of the electrostatic surface (Figure 3C). This would make negatively charged chloride binding electrostatically unfavorable. Alternatively, when the positively charged lysine side chain is present, the electrostatic environment becomes far more positive and therefore more conducive to chloride binding (Figures 3D and S9). Overall, the negatively charged E119 residue H-bonded to iron's equatorial-aqua ligand of complex **I** acts as an electrostatic lock that hinders chloride- and lysine-binding in the absence of the other. When both lysine and chloride are present, they disrupt the E119−aqua interaction and push E119 away from the Fe^{II} center (Figure 3E), transforming the electrostatic environment in the active site. Overall, our computational studies provide insights into the experimentally observed positive cooperativity between lysine- and chloride-binding events and reveal the role of E119 as an electrostatic lock in the active site assembly of BesD.

To experimentally verify the role of E119 as an electrostatic lock in BesD's active site, we used computationally guided rational protein design studies that systematically investigated the role of electrostatics in chloride-binding events. More specifically, we generated BesD variants with E119 mutated to Gln (E119Q BesD) and Ala (E119A BesD). Both the E119Q and E119A variants present a less negative electrostatic environment at the catalytic core compared to WT BesD and should favor the binding of negatively charged chloride to the iron center. Next, we measured the binding affinity of chloride to WT BesD and E119 mutants in the absence of any lysine. With an extremely weak K_d^{Cl} of 560 ± 15 mM, WT BesD required large nonphysiological levels of chloride to display binding-related UV−Vis signatures (Figures 3F and S10). On the other hand, the mutants E119Q (K_d^{Cl} = 83 ± 2 mM) and E119A (K_d^{Cl} = 40 ± 2 mM) demonstrate 6.7- and 14-fold stronger binding affinity for chloride, confirming the role

https://doi.org/10.1021/acscatal.3c02531
ACS Catal. 2023, 13, 13743−13755

of E119 as an electrostatic lock. Besides E119, BesD has two other negatively charged residues (D140 and D200) within 10 Å of the iron center that could also contribute to the negative electrostatics at the catalytic core (Figure S11). We note that BesD and HalD, both of which operate on positively charged substrates, are unique in terms of the richness of negatively charged residues in the vicinity of the catalytic core compared to other structurally characterized iron halogenases. Overall, these experimental findings combined with our computational studies offer new biochemical insights into how BesD utilizes residues around the catalytic core to manipulate the pocket electrostatic environment during the active site assembly to enable strong heterotropic cooperativity between the lysine- and chloride-binding events.

Having shown that the mutation of E119 to neutral residues mitigates electrostatic barriers to chloride binding, we next investigated its effect on lysine binding and chlorination catalysis. For this study, we dialyzed physiologically relevant levels of lysine against 0.43 ± 0.02 mM of WT BesD and designed E119Q and E119A variants under a total chloride concentration of 30 mM. At such chloride concentrations, we observe that lysine binds almost completely to WT BesD as expected but displays significantly diminished binding to E119Q and E119A variants (Figures 4A and S12). To investigate how these mutations impact the chlorination of lysine, we conducted activity assays with WT BesD and its E119Q and E119A variants. Reaction products were measured via UPLC-MS/MS, and the identity of BesD enzymatic products was confirmed by accurate mass measurements. UPLC-MRM chromatograms of the reaction products (Figures 4B and S14) demonstrate the presence of chlorinated lysine for WT BesD and E119 variants but with peak areas that are about an order of magnitude lower for the variants as compared to WT BesD (Figure 4C). Beyond chlorinated lysine, we also probed for and quantified unreacted lysine, the lactone/lactam form of lysine that may be formed by the cyclization of chlorinated lysine, and undesirable hydroxylated lysine side product (Figures S13 and S14). While the E119Q and E119A mutants show significant amounts of unreacted lysine, our analysis reveals that the reaction products are still mostly chlorinated lysine with some lysine lactam/lactone and negligible hydroxylated lysine (Figure S14D, a version of Figure 4C with the *y*-axis in the log scale). Notably, the relative ratio of the sum of chloro-lysine and lac-lysine generated via chlorination to hydroxy-lysine when measured in terms of their respective peak area ratio was found to be 28:1, 26:1, and 22:1 for WT, E119Q, and E119A, respectively. Therefore, while BesD variants retained their overall chemoselectivity profile, the desired catalytic yields are about an order of magnitude lower given their significantly reduced lysine-binding capability. Overall, these rational protein design-based binding and reactivity studies highlight the importance of a finely regulated electrostatic environment for the halogenation catalysis of charged substrates such as lysine.

Thus far, we have demonstrated that the electrostatic environment within the catalytic core of BesD can impact lysine and chloride binding, as well as chlorination yields. As such, electrostatic effects may also play an important role in determining the promiscuity of BesD in catalyzing C−H functionalization with anions beyond chloride. With this premise, we explored BesD's reactivity with other functionalizing anions such as bromide, azide, and nitrite. With bromide as the functionalizing anion, we detect two peaks in the MRM chromatogram that correspond to the mass transition associated with two regioisomers of brominated lysine (Figures 5A and S15). These peaks were absent in control reactions with no functionalizing anion or with chloride as the functionalizing anion. The identity of these peaks as brominated lysine was further confirmed via accurate mass measurements (Table S2). Therefore, we find that BesD is capable of functionalizing lysine with bromide, albeit with a low regioselectivity (Figure 5D). With azide as the functionalizing anion, we detect three peaks that correspond to three different regioisomers of azidated lysine based on the expected mass, controls, and accurate mass data (Figures 5B and S16). Similar to bromide, regioselectivity with azide is poor in BesD reactions with yields that are similar to what has been observed in other NHFe-Hals (Figure 5E).[10] With nitrite as the functionalizing anion, however, we detect no peak corresponding to nitrated lysine (Figures 5C,F and S17). Subsequent UV−Vis-based binding studies reveal that BesD is able to assemble its active site by recruiting both bromide and azide in the presence of lysine (Figure 5G,H) but is unable to recruit nitrite in a similar manner (Figure 5I). We speculate that the bent geometry of nitrite may position its positively charged nitrogen next to lysine's ammonium group, presenting an electrostatically unfavorable situation that inhibits the potential for positive heterotropic cooperative binding. We note that SyrB2, on the other hand, has been shown to exhibit significant promiscuity in binding a variety of functionalizing anions (bromide, azide, nitrite, cyanide, sulfide, cyanate, formate, and thiocyanate).[10] This likely arises from the fact that SyrB2 halogenase functionalizes neutral amino acids and possesses a positively charged R254 in the vicinity of the functionalizing anion-binding site (Figure S11). SyrB2's reactivity profile, however, is not as promiscuous as the anions it is able to bind, indicating that the binding stage of the catalytic cycle offers a lower degree of control in determining the C−H functionalization outcome. On the other hand, our studies show that when working with charged substrates like lysine, SCS and other residues in the vicinity of the catalytic center need to actively regulate the electrostatic environment to facilitate the charged substrate entry and positioning. Such complex electrostatic regulation at play with charged substrates would naturally give rise to novel heterotropic binding patterns with the functionalizing anion. This places greater restrictions on the geometry and distribution of charges on the functionalizing anion, as well. Consequently, such strict and complex electrostatic requirements needed for C−H functionalization of charged substrates endow the active site assembly stage with a high degree of control in determining the reaction promiscuity of BesD-like halogenases. In all, our studies provide pivotal insights needed for the design of modular non-heme iron enzymes that can functionalize positively charged substrates with anions, which will be important in future biocatalyst engineering campaigns.

CONCLUSIONS

How the electrostatic environment produced by the SCS of NHFe enzymes affects their catalysis is an ongoing area of investigation.[42,98−100] DFT calculations have shown that localized electric fields arising from charged residues and bound ions can impact the physicochemical properties, reactivities, and chemoselectivities of enzymatic systems.[41,99,101−103] Within this realm, our work on freestanding halogenases, BesD and HalB, updates the current under-

https://doi.org/10.1021/acscatal.3c02531
ACS Catal. 2023, 13, 13743−13755

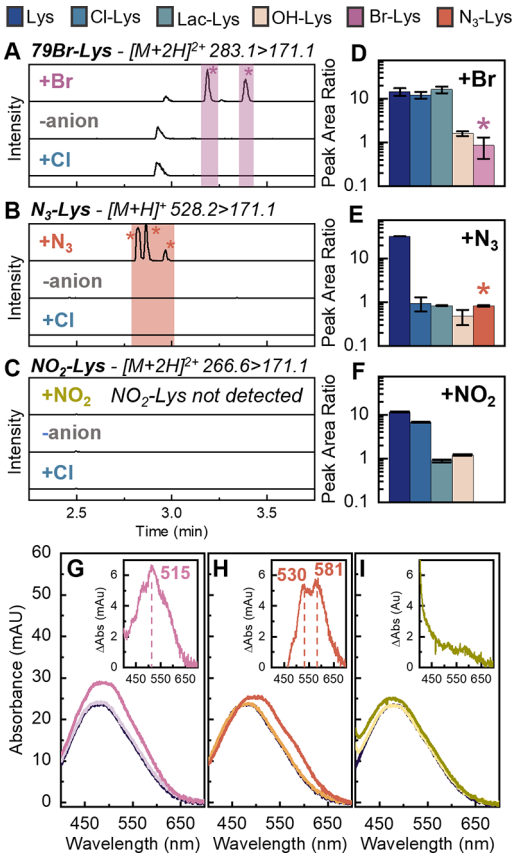

Figure 5. MRM chromatograms for mass transitions corresponding to (A) brominated lysine, (B) azidated lysine, or (C) nitrated lysine for 50 μM BesD reactions containing 5 mM 2OG, 1 mM sodium ascorbate, 100 μM $(NH_4)_2Fe(SO_4)_2$, and 200 μM lysine in 100 mM HEPES (pH = 7.5) with either 10 mM NaX (X = Br, N_3, NO_2), no anion added, or 5 mM NaCl added as indicated. Detected ion species and mass transitions are indicated at the top of each chromatogram set. Identity verification of analytes was accomplished with accurate mass measurements, as discussed in Materials and Methods. Peak area ratios (analyte/$^{13}C_6$,$^{15}N_2$-lysine internal standard) for reactions with (D) 10 mM NaBr, (E) 10 mM NaN_3, and (F) 10 mM $NaNO_2$. Asterisks on the chromatograms indicate peaks used to calculate brominated and azidated lysine peak areas. All detected products were AQC-derivatized analytes. Spectral changes in the MLCT band of 130 ± 5 μM BesD, 97.5 μM Fe, and 630 μM 2OG in 100 mM HEPES (pH = 7.5) upon sequential additions of 5 mM (G) NaBr, (H) NaN_3, or (I) $NaNO_2$, followed by the addition of 5 mM lysine.

standing of active site assembly with strong heterotropic cooperativity between the positively charged lysine and the chloride anion at play. Our computationally guided rational protein design studies offer unique insights into the role of a negatively charged E119 residue in the SCS of BesD-like halogenases that actively regulates catalytic pocket electrostatics to effectuate such cooperativity in the active site assembly. Mutations of the negatively charged E119 residue to polar Gln and neutral Ala result in an order-of-magnitude decrease in chlorination yields as the active site assembly is impaired in these mutants and highlights the importance of the binding stage in determining the overall catalysis performance. The importance of the binding stage of the catalytic cycle is also reflected in BesD's promiscuity to C−H functionalization, with non-native anions being impacted by its ability to bind with them. Such controls in BesD/HalB and other similar halogenases can foster greater conservation of cellular resources and prevent off-target reactions that lead to uncoupled consumption of O_2 in the chloro-bound form.[24] More generally, our studies highlight intricate electrostatic controls in freestanding halogenases that act upon charged substrates and are needed for tight binding and strategic positioning of the target C−H bond for effective functionalization. This is unlike the binding stages of SyrB2 and HctB halogenases where the substrate binding and positioning of target C−H bond are majorly controlled by protein−protein interactions (PPI) with partner proteins/domains to which the substrates are tethered. In turn, it would be interesting to investigate other freestanding NHFe-Hals that act upon charged substrates for novel electrostatic regulation of active site assembly along with implications for catalytic activity and reactivity profiles. These include positively charged ornithine halogenating HalD[39] and negatively charged adenine monophosphate halogenating AdaV.[25] Beyond the role of the electrostatic environment in controlling the active site assembly stage of these enzymes, it will also be interesting to use advanced DFT and QM/MM studies to explore how electrostatics impact the subsequent stages of oxygen activation, haloferryl formation, hydrogen abstraction, and halide transfer, all of which need to optimally work in tandem for the successful halogenation outcome. Ultimately, insights gleaned from these studies would be crucial for developing modular non-heme iron enzymes that act upon charged substrates like lysine and utilize functionalizing anions like chloride and beyond, paving the way for next-generation C−H functionalization biocatalysts.

■ ASSOCIATED CONTENT

Supporting Information

The Supporting Information is available free of charge at https://pubs.acs.org/doi/10.1021/acscatal.3c02531.

MRM transitions monitored for UPLC-MS/MS detection, accurate mass determination of enzymatic product, DFT-optimized geometries and RESP charges for various active site configurations; data on substrate anion cooperativity in HalB, AQC-derivatized lysine HPLC standard curve, equilibrium dialysis HPLC traces, chloride titration MLCT band spectra at various lysine concentrations, exact analysis of heterotrophic cooperativity in BesD, LOGOS plot for BesD-like halogenases and hydroxylases, structure snapshots from MD simulations, electrostatic surfaces for various active site forms, depiction of charged residues close to the active site in NHFe-Hals, representative chromatograms for mutant equilibrium dialysis, chlorinated lysine degradation pathway, UPLC-MRM chromatograms of activity assays, and gel of purified BesD and variants; detailed analysis of MD-simulated structures; and exact analysis of heterotropic cooperative binding in BesD (PDF)

■ AUTHOR INFORMATION

Corresponding Authors

Anoop Rama Damodaran − *Department of Chemistry, University of Minnesota, Twin Cities, Minneapolis, Minnesota 55455, United States*; Email: rdanoop@umn.edu

Ambika Bhagi-Damodaran − *Department of Chemistry, University of Minnesota, Twin Cities, Minneapolis, Minnesota 55455, United States*; orcid.org/0000-0002-4901-074X; Email: ambikab@umn.edu

https://doi.org/10.1021/acscatal.3c02531
ACS Catal. 2023, 13, 13743−13755

Authors

Elizabeth R. Smithwick − *Department of Chemistry, University of Minnesota, Twin Cities, Minneapolis, Minnesota 55455, United States*

R. Hunter Wilson − *Department of Chemistry, University of Minnesota, Twin Cities, Minneapolis, Minnesota 55455, United States*

Sourav Chatterjee − *Department of Chemistry, University of Minnesota, Twin Cities, Minneapolis, Minnesota 55455, United States*

Yu Pu − *Department of Chemistry, University of Minnesota, Twin Cities, Minneapolis, Minnesota 55455, United States*

Joseph J. Dalluge − *Department of Chemistry, University of Minnesota, Twin Cities, Minneapolis, Minnesota 55455, United States*

Complete contact information is available at: https://pubs.acs.org/10.1021/acscatal.3c02531

Author Contributions

E.R.S., A.R.D., and A.B.D. designed the study. E.R.S. performed all experimental studies and DFT studies and analyzed all data. R.H.W. performed MD simulations. S.C. and J.J.D. designed and helped execute the activity assays. Y.P. helped purify proteins. A.R.D. and A.B.D. supervised the study. E.R.S., A.R.D., and A.B.D. wrote the manuscript with contributions from all authors. All authors have given approval to the final version of the manuscript.

Funding

E.R.S. and R.H.W. acknowledge the support of the National Institute of Health Chemical Biology Training Grant (T32GM132029). The halogenation part of this work was supported by NSF CBET-2046527). The azidation/nitration/hydroxylation part of this work was supported by the Regents of the University of Minnesota. Mass spectrometry analysis was performed at The University of Minnesota Department of Chemistry Mass Spectrometry Laboratory (MSL), supported by the Office of the Vice President of Research, College of Science and Engineering, and the Department of Chemistry at the University of Minnesota, as well as The National Science Foundation (NSF, Award CHE-1336940).

Notes

The authors declare no competing financial interest.

■ ACKNOWLEDGMENTS

The authors would like to thank Prof. Michelle Chang (U.C. Berkeley) for BesD and HalB plasmids. All color palettes for figures were taken from ref 104.

■ ABBREVIATIONS

NHFe-Hals, non-heme iron halogenases; NHFe-Hyds, non-heme iron hydroxylases; 2OG, 2-oxoglutarate; PCS, primary coordination sphere; SCS, secondary coordination sphere; MLCT, metal-to-ligand charge transfer; AQC, 6-amino-quinolyl-*N*-hydroxysuccinimidyl carbamate

■ REFERENCES

(1) Bornscheuer, U. T.; Huisman, G. W.; Kazlauskas, R. J.; Lutz, S.; Moore, J. C.; Robins, K. Engineering the Third Wave of Biocatalysis. *Nature* **2012**, *485*, 185.

(2) Hanefeld, U.; Hollmann, F.; Paul, C. E. Biocatalysis Making Waves in Organic Chemistry. *Chem. Soc. Rev.* **2022**, *51*, 594.

(3) Chapman, J.; Ismail, A. E.; Dinu, C. Z. Industrial Applications of Enzymes: Recent Advances, Techniques, and Outlooks. *Catalysts* **2018**, *8* (6), 20−29.

(4) Tian, J.; Garcia, A. A.; Donnan, P. H.; Bridwell-Rabb, J. Leveraging a Structural Blueprint to Rationally Engineer the Rieske Oxygenase TsaM. *Biochemistry* **2023**, *62*, 1807.

(5) Wang, Y.; Davis, I.; Shin, I.; Xu, H.; Liu, A. Molecular Rationale for Partitioning between C-H and C-F Bond Activation in Heme-Dependent Tyrosine Hydroxylase. *J. Am. Chem. Soc.* **2021**, *143* (12), 4680−4693.

(6) Lewis, J. C.; Coelho, P. S.; Arnold, F. H. Enzymatic Functionalization of Carbon−Hydrogen Bonds. *Chem. Soc. Rev.* **2011**, *40* (4), 2003−2021.

(7) Neugebauer, M. E.; Sumida, K. H.; Pelton, J. G.; McMurry, J. L.; Marchand, J. A.; Chang, M. C. Y. A Family of Radical Halogenases for the Engineering of Amino-Acid-Based Products. *Nat. Chem. Biol.* **2019**, *15* (10), 1009−1016.

(8) Vaillancourt, F. H.; Vosburg, D. A.; Walsh, C. T. Dichlorination and Bromination of a Threonyl- S -Carrier Protein by the Non-Heme Fe(II) Halogenase SyrB2. *ChemBioChem* **2006**, *7*, 748−752.

(9) Büchler, J.; Malca, S. H.; Patsch, D.; Voss, M.; Turner, N. J.; Bornscheuer, U. T.; Allemann, O.; Le Chapelain, C.; Lumbroso, A.; Loiseleur, O.; et al. Algorithm-Aided Engineering of Aliphatic Halogenase WelO5* for the Asymmetric Late-Stage Functionalization of Soraphens. *Nat. Commun.* **2022**, *13* (1), 371.

(10) Matthews, M. L.; Chang, W. C.; Layne, A. P.; Miles, L. A.; Krebs, C.; Bollinger, J. M. Direct Nitration and Azidation of Aliphatic Carbons by an Iron-Dependent Halogenase. *Nat. Chem. Biol.* **2014**, *10* (3), 209−215.

(11) Kim, C. Y.; Mitchell, A. J.; Glinkerman, C. M.; Li, F.; Puskal, T.; Weng, J.-K. The Chloroalkaloid (−)-Acutumine Is Biosynthesized via a Fe(II)- and 2-Oxoglutarate- Dependent Halogenase in Menispermaceae Plants. *Nat. Commun.* **2020**, *11*, 1867.

(12) Zhu, Q.; Hillwig, M. L.; Doi, Y.; Liu, X. Aliphatic Halogenase Enables Late-Stage C-H Functionalization: Selective Synthesis of a Brominated Fischerindole Alkaloid with Enhanced Antibacterial Activity. *ChemBioChem* **2016**, *17* (6), 466−470.

(13) Vaillancourt, F. H.; Yin, J.; Walsh, C. T. SyrB2 in Syringomycin E Biosynthesis Is a Nonheme FeII α-Ketoglutarate- and O2-Dependent Halogenase. *Proc. Natl. Acad. Sci. U. S. A.* **2005**, *102* (29), 10111−10116.

(14) Pratter, S. M.; Light, K. M.; Solomon, E. I.; Straganz, G. D. The Role of Chloride in the Mechanism of O2 Activation at the Mononuclear Nonheme Fe(II) Center of the Halogenase HctB. *J. Am. Chem. Soc.* **2014**, *136*, 9385−9395.

(15) Neugebauer, M. E.; Sumida, K. H.; Pelton, J. G.; Mcmurry, J. L.; Marchand, J. A.; Chang, M. C. Y. A Family of Radical Halogenases for the Engineering of Amino-Acid-Based Products. *Nat. Chem. Biol.* **2019**, *15*, 1009−1016.

(16) Matthews, M. L.; Neumann, C. S.; Miles, L. A.; Grove, T. L.; Booker, S. J.; Krebs, C.; Walsh, C. T.; Bollinger, J. M. Substrate Positioning Controls the Partition between Halogenation and Hydroxylation in the Aliphatic Halogenase, SyrB2. *Proc. Natl. Acad. Sci. U. S. A.* **2009**, *106* (42), 17723−17728.

(17) Jiang, W.; Heemstra, J. R.; Forseth, R. R.; Neumann, C. S.; Manaviazar, S.; Schroeder, F. C.; Hale, K. J.; Walsh, C. T. Biosynthetic Chlorination of the Piperazate Residue in Kutzneride Biosynthesis by KthP. *Biochemistry* **2011**, *50* (27), 6063−6072.

(18) Ueki, M.; Galonić, D. P.; Vaillancourt, F. H.; Garneau-Tsodikova, S.; Yeh, E.; Vosburg, D. A.; Schroeder, F. C.; Osada, H.; Walsh, C. T. Enzymatic Generation of the Antimetabolite γ,γ-Dichloroaminobutyrate by NRPS and Mononuclear Iron Halogenase Action in a Streptomycete. *Chem. Biol.* **2006**, *13*, 1183−1191.

(19) Pratter, S. M.; Ivkovic, J.; Birner-Gruenberger, R.; Breinbauer, R.; Zangger, K.; Straganz, G. D. More than Just a Halogenase: Modification of Fatty Acyl Moieties by a Trifunctional Metal Enzyme. *ChemBioChem* **2014**, *15*, 567−574.

(20) Dheerja, K.; Wang, B.; Gu, L.; Razelun, J.; Sherman, D. H.; Gerwick, W. H.; Hakansson, K.; Smith, J. L. Conformational Switch

Triggered by α-Ketoglutarate in a Halogenase of Curacin A Biosynthesis. *Proc. Natl. Acad. Sci. U. S. A.* **2010**, *107* (32), 14099−14104.
(21) Galonić, D. P.; Vaillancourt, F. H.; Walsh, C. T. Halogenation of Unactivated Carbon Centers in Natural Product Biosynthesis: Trichlorination of Leucine during Barbamide Biosynthesis. *J. Am. Chem. Soc.* **2006**, *128* (12), 3900−3901.
(22) Fraley, A. E.; Dell, M.; Schmalhofer, M.; Meoded, R. A.; Bergande, C.; Groll, M.; Piel, J. Heterocomplex Structure of a Polyketide Synthase Component Involved in Modular Backbone Halogenation. *Structure* **2023**, *31* (5), 565−572.e4.
(23) Vaillancourt, F. H.; Yeh, E.; Vosburg, D. A.; O'Connor, S. E.; Walsh, C. T. Cryptic Chlorination by a Non-Haem Iron Enzyme during Cyclopropyl Amino Acid Biosynthesis. *Nature* **2005**, *436* (7054), 1191−1194.
(24) Hillwig, M. L.; Liu, X. A New Family of Iron-Dependent Halogenases Acts on Freestanding Substrates. *Nat. Chem. Biol.* **2014**, *10* (11), 921−923.
(25) Zhang, Y.; Zhao, C.; Yan, S.; Li, Q.; Zhu, H.; Zhong, Z.; Ye, Y.; Deng, Z. An $Iron^{2+}$- and α-Ketoglutarate-Dependent Halogenase Acts on Nucleotide Substrates. *Angew. Chem., Int. Ed.* **2020**, *59*, 9478.
(26) Papadopoulou, A.; Meierhofer, J.; Meyer, F.; Hayashi, T.; Schneider, S.; Sager, E.; Buller, R. Re-Programming and Optimization of a L-Proline Cis-4-Hydroxylase for the Cis-3-Halogenation of Its Native Substrate. *ChemCatChem* **2021**, 1−7.
(27) Mitchell, A. J.; Dunham, N. P.; Bergman, J. A.; Wang, B.; Zhu, Q.; Chang, W. C.; Liu, X.; Boal, A. K. Structure-Guided Reprogramming of a Hydroxylase to Halogenate Its Small Molecule Substrate. *Biochemistry* **2017**, *56* (3), 441−444.
(28) Neugebauer, M. E.; Kissman, E. N.; Marchand, J. A.; Pelton, J. G.; Sambold, N. A.; Millar, D. C.; Chang, M. C. Y. Reaction Pathway Engineering Converts a Radical Hydroxylase into a Halogenase. *Nat. Chem. Biol.* **2022**, *18*, 171−179.
(29) Hangasky, J. A.; Taabazuing, C. Y.; Valliere, M. A.; Knapp, M. J. Imposing Function down a (Cupin)-Barrel: Secondary Structure and Metal Stereochemistry in the αKG-Dependent Oxygenases. *Metallomics* **2013**, *5* (4), 287−301.
(30) Blasiak, L. C.; Vaillancourt, F. H.; Walsh, C. T.; Drennan, C. L. Crystal Structure of the Non-Haem Iron Halogenase SyrB2 in Syringomycin Biosynthesis. *Nature* **2006**, *440* (7082), 368−371.
(31) Chaplin, V. D.; Hangasky, J. A.; Huang, H. T.; Duan, R.; Maroney, M. J.; Knapp, M. J. Chloride Supports O_2 Activation in the D201G Facial Triad Variant of Factor-Inhibiting Hypoxia Inducible Factor, an α-Ketoglutarate Dependent Oxygenase. *Inorg. Chem.* **2018**, *57* (20), 12588−12595.
(32) Gorres, K. L.; Pua, K. H.; Raines, R. T. Stringency of the 2-His-1-Asp Active-Site Motif in Prolyl 4-Hydroxylase. *PLoS One* **2009**, *4* (11), 1−6.
(33) Grzyska, P. K.; Müller, T. A.; Campbell, M. G.; Hausinger, R. P. Metal Ligand Substitution and Evidence for Quinone Formation in Taurine/α-Ketoglutarate Dioxygenase. *J. Inorg. Biochem.* **2007**, *101* (5), 797−808.
(34) Mehmood, R.; Vennelakanti, V.; Kulik, H. J. Spectroscopically Guided Simulations Reveal Distinct Strategies for Positioning Substrates to Achieve Selectivity in Nonheme Fe(II)/α-Ketoglutarate-Dependent Halogenases. *ACS Catal.* **2021**, *11* (19), 12394−12408.
(35) Mehmood, R.; Qi, H. W.; Steeves, A. H.; Kulik, H. J. The Protein's Role in Substrate Positioning and Reactivity for Biosynthetic Enzyme Complexes: The Case of SyrB2/SyrB1. *ACS Catal.* **2019**, *9* (6), 4930−4943.
(36) Wilson, R. H.; Chatterjee, S.; Smithwick, E. R.; Dalluge, J. J.; Bhagi-damodaran, A. Role of a Secondary Coordination Sphere Residue in Halogenation Catalysis of Non-Heme Iron Enzymes. *ACS Catal.* **2022**, *12*, 10913−10924.
(37) Wong, S. D.; Srnec, M.; Matthews, M. L.; Liu, L. V.; Kwak, Y.; Park, K.; Bell, C. B.; Alp, E. E.; Zhao, J.; Yoda, Y.; et al. Elucidation of the Fe(IV)═O Intermediate in the Catalytic Cycle of the Halogenase SyrB2. *Nature* **2013**, *499* (7458), 320−323.
(38) Kastner, D. W.; Nandy, A.; Mehmood, R.; Kulik, H. J. Mechanistic Insights Into Substrate Positioning That Distinguish Non-heme Fe(II)/α-Ketoglutarate-Dependent Halogenases and Hydroxylases. *ACS Catal.* **2023**, *13*, 2489−2501.
(39) Kissman, E. N.; Neugebauer, M. E.; Sumida, K. H.; Swenson, C. V.; Nicholas, A.; Marchand, J. A.; Millar, D. C.; Chang, M. C. Y. Biocatalytic control of site-selectivity and chain length-selectivity in radical amino acid halogenases. *Proc. Natl. Acad. Sci. U. S. A.* **2023**, *120*, No. e2214512120.
(40) Martinie, R. J.; Livada, J.; Chang, W.; Green, M. T.; Krebs, C.; Bollinger, J. M.; Silakov, A. Experimental Correlation of Substrate Position with Reaction Outcome in the Aliphatic Halogenase, SyrB2. *J. Am. Chem. Soc.* **2015**, *137*, 6912−6919.
(41) Timmins, A.; Fowler, N. J.; Warwicker, J.; Straganz, G. D.; de Visser, S. P. Does Substrate Positioning Affect the Selectivity and Reactivity in the Hectochlorin Biosynthesis Halogenase? *Front. Chem.* **2018**, *6*, 513.
(42) Timmins, A.; De Visser, S. P. Enzymatic Halogenases and Haloperoxidases: Computational Studies on Mechanism and Function. In *Advances in Protein Chemistry and Structural Biology*; Elsevier Inc., 2015; pp 113−151.
(43) Solomon, E. I.; Deweese, D. E.; Babicz, T. Mechanisms of O_2 Activation by Mononuclear Non-Heme Iron Enzymes. *Biochemistry* **2021**, *60*, 3497−3506.
(44) Matthews, M. L.; Krest, C. M.; Barr, E. W.; Vaillancourt, H.; Walsh, C. T.; Green, M. T.; Krebs, C.; Bollinger, J. M. Substrate-Triggered Formation and Remarkable Stability of the C-H Bond-Cleaving Chloroferryl Intermediate in the Aliphatic Halogenase, SyrB2. *Biochemistry* **2009**, *48*, 4331−4343.
(45) Solomon, E. I.; Goudarzi, S.; Sutherlin, K. D. O_2 Activation by Non-Heme Iron Enzymes. *Biochemistry* **2016**, *55* (46), 6363−6374.
(46) Light, K. M.; Hangasky, J. A.; Knapp, M. J.; Solomon, E. I. Spectroscopic Studies of the Mononuclear Non-Heme Fe^{II} Enzyme FIH: Second-Sphere Contributions to Reactivity. *J. Am. Chem. Soc.* **2013**, *135*, 9665−9674.
(47) Neidig, M. L.; Brown, C. D.; Light, K. M.; Fujimori, D. G.; Nolan, E. M.; Price, J. C.; Barr, E. W.; Bollinger, J. M.; Krebs, C.; Walsh, C. T.; et al. CD and MCD of CytC3 and Taurine Dioxygenase: Role of the Facial Triad in α-KG-Dependent Oxygenases. *J. Am. Chem. Soc.* **2007**, *129* (46), 14224−14231.
(48) Iyer, S. R.; Chaplin, V. D.; Knapp, M. J.; Solomon, E. I. O2 Activation by Nonheme Fe^{II} α-Ketoglutarate-Dependent Enzyme Variants: Elucidating the Role of the Facial Triad Carboxylate in FIH. *J. Am. Chem. Soc.* **2018**, *140*, 11777−11783.
(49) Kal, S.; Que, L. Dioxygen Activation by Nonheme Iron Enzymes with the 2-His-1-Carboxylate Facial Triad That Generate High-Valent Oxoiron Oxidants. *J. Biol. Inorg. Chem.* **2017**, *22* (2−3), 339−365.
(50) Waterhouse, A.; Bertoni, M.; Bienert, S.; Studer, G.; Tauriello, G.; Gumienny, R.; Heer, F. T.; De Beer, T. A. P.; Rempfer, C.; Bordoli, L.; et al. SWISS-MODEL: Homology Modelling of Protein Structures and Complexes. *Nucleic Acids Res.* **2018**, *46* (W1), W296−W303.
(51) Bienert, S.; Waterhouse, A.; De Beer, T. A. P.; Tauriello, G.; Studer, G.; Bordoli, L.; Schwede, T. The SWISS-MODEL Repository — New Features and Functionality. *Nucleic Acids Res.* **2017**, *45*, 313−319.
(52) Bertoni, M.; Kiefer, F.; Biasini, M.; Bordoli, L.; Schwede, T. Modeling Protein Quaternary Structure of Homo- and Hetero-Oligomers beyond Binary Interactions by Homology. *Sci. Rep.* **2017**, *7*, 1−15.
(53) Guex, N.; Peitsch, M. C.; Schwede, T. Automated Comparative Protein Structure Modeling with SWISS-MODEL and Swiss-PdbViewer: A Historical Perspective. *Electrophoresis* **2009**, *30*, S162−S173.
(54) Studer, G.; Rempfer, C.; Waterhouse, A. M.; Gumienny, R.; Haas, J.; Schwede, T. QMEANDisCo — Distance Constraints Applied on Model Quality Estimation. *Bioinformatics* **2020**, *36* (6), 1765−1771.

https://doi.org/10.1021/acscatal.3c02531
ACS Catal. 2023, 13, 13743−13755

(55) Waterhouse, A.; Bertoni, M.; Bienert, S.; Studer, G.; Tauriello, G.; Gumienny, R.; Heer, F. T.; De Beer, T. A. P.; Rempfer, C.; Bordoli, L.; et al. SWISS-MODEL: Homology Modelling of Protein Structures and Complexes. *Nucleic Acids Res.* **2018**, *46*, 296−303.
(56) Gordon, J. C.; Myers, J. B.; Folta, T.; Shoja, V.; Heath, L. S.; Onufriev, A. H + +: A Server for Estimating p K_a s and Adding Missing Hydrogens to Macromolecules. *Nucleic Acids Res.* **2005**, *33*, 368−371.
(57) Anandakrishnan, R.; Aguilar, B.; Onufriev, A. V. H++ 3.0: Automating PK Prediction and the Preparation of Biomolecular Structures for Atomistic Molecular Modeling and Simulations. *Nucleic Acids Res.* **2012**, *40*, 537−541.
(58) Myers, J.; Grothaus, G.; Narayanan, S.; Onufriev, A. A Simple Clustering Algorithm Can Be Accurate Enough for Use in Calculations of PKs in Macromolecules. *Proteins, Struct., Funct., Bioinf.* **2006**, *63*, 928−938.
(59) Case, D. A.; Belfon, K.; Ben-Shalom, I. Y.; Brozell, S. R.; Cerutti, D. S.; Cheatham, T. E. I.; Cruzeiro, V. W. D.; Darden, T. A.; Duke, R. E.; Giambasu, G.; *AMBER 2020*; University of California: San Francisco, 2020.
(60) Tian, C.; Kasavajhala, K.; Belfon, K. A. A.; Raguette, L.; Huang, H.; Migues, A.; Bickel, J.; Wang, Y.; Pincay, J.; Wu, Q.; et al. Ff19SB: Amino-Acid-Specific Protein Backbone Parameters Trained against Quantum Mechanics Energy Surfaces in Solution. *J. Chem. Theory Comput.* **2020**, *16*, 528−552.
(61) Wang, J.; Wolf, R. M.; Caldwell, J. W.; Kollman, P. A.; Case, D. A. Development and Testing of a General AMBER Force Field. *J. Comput. Chem.* **2004**, *25* (9), 1157−1174.
(62) Li, Z.; Song, L. F.; Li, P.; Merz, K. M. Systematic Parametrization of Divalent Metal Ions for the OPC3, OPC, TIP3P-FB, and TIP4P-FB Water Models. *J. Chem. Theory Comput.* **2020**, *16*, 4429−4442.
(63) Wang, J.; Wang, W.; Kollman, P. A.; Case, D. A. Automatic Atom Type and Bond Type Perception in Molecular Mechanical Calculations. *J. Mol. Graph. Model.* **2006**, *25*, 247−260.
(64) Izadi, S.; Anandakrishnan, R.; Onufriev, A. V. Building Water Models: A Different Approach. *J. Phys. Chem. Lett.* **2014**, *5*, 3863−3871.
(65) Horn, A. H. C. A Consistent Force Field Parameter Set for Zwitterionic Amino Acid Residues. *J. Mol. Model.* **2014**, *20*, 2478.
(66) Li, P.; Merz, K. M. MCPB.Py: A Python Based Metal Center Parameter Builder. *J. Chem. Inf. Model.* **2016**, *56* (4), 599−604.
(67) Case, D. A.; Aktulga, H. M.; Belfon, K.; Ben-Shalom, I. Y.; Brozell, S. R.; Cerutti, D. S.; Cheatham, T. E. I.; Cisneros, G. A.; Cruzeiro, V. W. D.; Darden, T. A.; *Amber 2021*; University of California: San Francisco, 2021.
(68) Becke, A. D. Density-Functional Thermochemistry. III. The Role of Exact Exchange. *J. Chem. Phys.* **1993**, *98* (7), 5648−5652.
(69) Wilk, L.; Nusair, M. Accurate Spin-Dependent Electron Liquid Correlation Energies for Local Spin Density Calculations: A Critical Analysis1. *Can. J. Phys.* **1980**, *58*, 1200−1211.
(70) Lee, C.; Yang, W.; Parr, R. G. Development of the Colic-Salvetti Correlation-Energy into a Functional of the Electron Density. *Phys. Rev. B* **1988**, *37* (2), 785−789.
(71) Roe, D. R.; Cheatham, T. E. PTRAJ and CPPTRAJ: Software for Processing and Analysis of Molecular Dynamics Trajectory Data. *J. Chem. Theory Comput.* **2013**, *9*, 3084−3095.
(72) Nicholls, A. Confidence Limits, Error Bars and Method Comparison in Molecular Modeling. Part 1: The Calculation of Confidence Intervals. *J. Comput. Aided Mol. Des.* **2014**, *26*, 887−918.
(73) Neese, F. The ORCA Program System. *Wiley Interdiscip. Rev.: Comput. Mol. Sci.* **2012**, *2*, 73−78.
(74) Neese, F. Software Update: The ORCA Program System — Version 5.0. *Wiley Interdiscip. Rev.: Comput. Mol. Sci.* **2022**, *12*, 1−15.
(75) Grimme, S.; Ehrlich, S.; Goerigk, L. Effect of the Damping Function in Dispersion Corrected Density Functional Theory. *J. Comput. Chem.* **2011**, *32* (7), 1456−1465.
(76) Schäfer, A.; Horn, H.; Ahlrichs, R. Fully Optimized Contracted Gaussian Basis Sets for Atoms Li to Kr. *J. Chem. Phys.* **1992**, *97* (4), 2571−2577.
(77) Schafer, A.; Huber, C.; Ahlrichs, R. Fully Optimized Contracted Gaussian Basis Sets of Triple Zeta Valence Quality for Atoms Li to Kr. *J. Chem. Phys.* **1994**, *100* (8), 5829−5835.
(78) Phys, J. C.; Grimme, S.; Antony, J.; Ehrlich, S. Parametrization of Density Functional Dispersion Correction (DFT-D) for the 94 Elements H-Pu Dispersion Correction DFT-D··· for the 94 Elements H-Pu. *J. Chem. Phys.* **2010**, *132* (15), 154104−154118.
(79) Smith, D. G. A.; Burns, L. A.; Patkowski, K.; Sherrill, C. D. Revised Damping Parameters for the D3 Dispersion Correction to Density Functional Theory. *J. Phys. Chem. Lett.* **2016**, *7*, 2197−2203.
(80) Weigend, F. Accurate Coulomb-Fitting Basis Sets for H to Rn. *Phys. Chem. Chem. Phys.* **2006**, *8* (9), 1057−1065.
(81) Lu, T.; Chen, F. Multiwfn: A Multifunctional Wavefunction Analyzer. *J. Comput. Chem.* **2012**, *33* (5), 580−592.
(82) Zhang, J.; Lu, T. Efficient Evaluation of Electrostatic Potential with Computerized Optimized Code. *Phys. Chem. Chem. Phys.* **2021**, *23* (36), 20323−20328.
(83) Lu, T.; Chen, F. Quantitative Analysis of Molecular Surface Based on Improved Marching Tetrahedra Algorithm. *J. Mol. Graph. Model.* **2012**, *38*, 314−323.
(84) Humphrey, W.; Dalke, A.; Schulten, K. VMD - Visual Molecular Dynamics. *J. Mol. Graph.* **1996**, *14*, 33−38.
(85) Edgar, R. C. MUSCLE: A Multiple Sequence Alignment Method with Reduced Time and Space Complexity. *BMC Bioinf.* **2004**, *5*, 1−19.
(86) Fu, L.; Niu, B.; Zhu, Z.; Wu, S.; Li, W. CD-HIT: Accelerated for Clustering the next-Generation Sequencing Data. *Bioinformatics* **2012**, *28* (23), 3150−3152.
(87) Li, W.; Godzik, A. Cd-Hit: A Fast Program for Clustering and Comparing Large Sets of Protein or Nucleotide Sequences. *Bioinformatics* **2006**, *22* (13), 1658−1659.
(88) Crooks, G.; Hon, G.; Chandonia, J.; Brenner, S. WebLogo: A Sequence Logo Generator. *Genome Res.* **2004**, *14*, 1188−1190.
(89) Ryle, M. J.; Padmakumar, R.; Hausinger, R. P. Stopped-Flow Kinetic Analysis of Escherichia Coli Taurine/α- Ketoglutarate Dioxygenase: Interactions with α-Ketoglutarate, Taurine, and Oxygen. *Biochemistry* **1999**, *38* (46), 15278−15286.
(90) Price, J. C.; Barr, E. W.; Tirupati, B.; Bollinger, J. M.; Krebs, C. The First Direct Characterization of a High-Valent Iron Intermediate in the Reaction of an α-Ketoglutarate-Dependent Dioxygenase: A High-Spin Fe(IV) Complex in Taurine/α-Ketoglutarate Dioxygenase (TauD) from Escherichia Coli. *Biochemistry* **2003**, *42* (24), 7497−7508.
(91) Ho, R. Y. N.; Mehn, M. P.; Hegg, E. L.; Liu, A.; Ryle, M. J.; Hausinger, R. P.; Que, L. Resonance Raman Studies of the Iron(II)-α-Keto Acid Chromophore in Model and Enzyme Complexes. *J. Am. Chem. Soc.* **2001**, *123* (21), 5022−5029.
(92) Saban, E.; Chen, Y. H.; Hangasky, J. A.; Taabazuing, C. Y.; Holmes, B. E.; Knapp, M. J. The Second Coordination Sphere of FIH Controls Hydroxylation. *Biochemistry* **2011**, *50* (21), 4733−4740.
(93) Mondal, P.; Rajapakse, S.; Wijeratne, G. B. Following Nature's Footprint: Mimicking the High-Valent Heme-Oxo Mediated Indole Monooxygenation Reaction Landscape of Heme Enzymes. *J. Am. Chem. Soc.* **2022**, *144* (9), 3843−3854.
(94) Caranto, J. D.; Weitz, A.; Hendrich, M. P.; Kurtz, D. M. The Nitric Oxide Reductase Mechanism of a Flavo-Diiron Protein: Identification of Active-Site Intermediates and Products. *J. Am. Chem. Soc.* **2014**, *136* (22), 7981−7992.
(95) Hosseinzadeh, P.; Marshall, N. M.; Chacón, K. N.; Yu, Y.; Nilges, M. J.; New, S. Y.; Tashkov, S. A.; Blackburn, N. J.; Lu, Y. Design of a Single Protein That Spans the Entire 2-V Range of Physiological Redox Potentials. *Proc. Natl. Acad. Sci. U. S. A.* **2016**, *113* (2), 262−267.
(96) Velazquez-Campoy, A.; Goñi, G.; Peregrina, J. R.; Medina, M. Exact Analysis of Heterotropic Interactions in Proteins: Character-

ization of Cooperative Ligand Binding by Isothermal Titration Calorimetry. *Biophys. J.* **2006**, *91* (5), 1887−1904.
(97) Guo, A. C. ECMDB: The E. Coli Metabolome Database. *Nucleic Acids Res.* **2013**, *41*, D625−D630.
(98) Ali, H. S.; Henchman, R. H.; Warwicker, J.; De Visser, S. P. How Do Electrostatic Perturbations of the Protein Affect the Bifurcation Pathways of Substrate Hydroxylation versus Desaturation in the Nonheme Iron-Dependent Viomycin Biosynthesis Enzyme? *J. Phys. Chem. A* **2021**, *125* (8), 1720−1737.
(99) Lin, Y. T.; Ali, H. S.; de Visser, S. P. Electrostatic Perturbations from the Protein Affect C−H Bond Strengths of the Substrate and Enable Negative Catalysis in the TmpA Biosynthesis Enzyme. *Chem. − Eur. J.* **2021**, *27* (34), 8851−8864.
(100) Wojdyla, Z.; Borowski, T. Properties of the Reactants and Their Interactions within and with the Enzyme Binding Cavity Determine Reaction Selectivities. The Case of Fe(II)/2-Oxoglutarate Dependent Enzymes. *Chem. − Eur. J.* **2022**, *28* (18), No. e202104106.
(101) De Visser, S. P. On the Relationship between Internal Energy and Both the Polarizability Volume and the Diamagnetic Susceptibility. *Phys. Chem. Chem. Phys.* **1999**, *1* (5), 749−753.
(102) Shaik, S.; Ramanan, R.; Danovich, D.; Mandal, D. Structure and Reactivity/Selectivity Control by Oriented-External Electric Fields. *Chem. Soc. Rev.* **2018**, *47* (14), 5125−5145.
(103) Shaik, S.; De Visser, S. P.; Kumar, D. External Electric Field Will Control the Selectivity of Enzymatic-like Bond Activations. *J. Am. Chem. Soc.* **2004**, *126* (37), 11746−11749.
(104) Crameri, F.; Shephard, G. E.; Heron, P. J. The Misuse of Colour in Science Communication. *Nat. Commun.* **2020**, *11* (1), 1−10.

https://doi.org/10.1021/acscatal.3c02531
ACS Catal. 2023, 13, 13743−13755